Evolution of a Jet-in-Coflow

Sampat, Rishikesh; Schrijer, Ferry; Gangoli Rao, Arvind

DOI
10.1007/s10494-025-00648-5

Publication date
2025

Document Version
Final published version

Published in
Flow, Turbulence and Combustion

Citation (APA)
Sampat, R., Schrijer, F., & Gangoli Rao, A. (2025). Evolution of a Jet-in-Coflow. *Flow, Turbulence and Combustion*, Article 068103. https://doi.org/10.1007/s10494-025-00648-5

Flow, Turbulence and Combustion
https://doi.org/10.1007/s10494-025-00648-5

RESEARCH

Evolution of a Jet-in-Coflow

Rishikesh Sampat[1] · **Ferry Schrijer**[1] · **Gangoli Rao Arvind**[1]

Received: 18 September 2024 / Accepted: 23 February 2025

Abstract

The jet-in-coflow is a two-stream configuration having engineering applications in combustors and gas turbine engine exhausts. In practical systems, the coflow generates a boundary layer of the outer wall of the jet pipe and may also have a certain level of turbulence. In the current work, the evolution of this flow configuration is studied using an air-air turbulent jet in a low turbulence coflow (turbulence intensity $< 6\%$), and the 2D velocity field is measured by planar particle image velocimetry. Cases of varying coflow ratio (ratio of coflow velocity to jet velocity) of 0 (turbulent free jet), 0.09, 0.15, and 0.33 are generated by keeping a constant velocity jet ($Re = 14000$) and varying the coflow velocity. The trends of jet centerline properties such as velocity decay, jet spread, and jet momentum of jet-in-coflow cases, scaled to represent an equivalent free jet, show deviations from that of the turbulent free jet. The radial profile of mean velocity shows a region of velocity deficit, compared to a turbulent free jet, on the coflow side in the jet-in-coflow cases. In contrast, the turbulence intensity and Reynolds shear stress profiles show an enhanced peak near the interface for the jet-in-coflow cases. Further, conditional statistics were extracted by detecting the interface between the jet and the surroundings, wherein the same trends are observed. The low turbulence levels of the coflow have little effect on the jet/coflow interface, as seen by the conditional enstrophy diffusion and tortuosity compared to a turbulent free jet. The differences at the jet/coflow interface of a jet-in-coflow with respect to a turbulent free jet are attributed to the boundary layer initially developed by the turbulent coflow over the pipe generating the jet, and these are seen throughout the near-to-intermediate field ($0 \leq x/D \leq 40$).

Keywords Jet-in-coflow · Turbulent interface · Conditional statistics

---

These authors contributed equally to this work.

✉ Rishikesh Sampat
r.p.sampat@tudelft.nl

Ferry Schrijer
f.f.j.schrijer@tudelft.nl

Gangoli Rao Arvind
a.gangolirao@tudelft.nl

[1] Flow Physics and Technology, Faculty of Aerospace Engineering, TU Delft, Kluyverweg 1, 2629HS Delft, The Netherlands

1 Introduction

The turbulent-jet-in-turbulent-coflow is a configuration in which a turbulent jet is surrounded by a turbulent coflow. Studying the flow physics can help in understanding the nature of mixing between the two streams. This finds application in combustion devices, such as those used to create Flameless/MILD combustion conditions for low NO_x emission production. The Delft Jet in hot coflow (Oldenhof et al. 2011) and Cabra flame (Cabra et al. 2005) are examples where this configuration is used with a coflow ratio (ratio of coflow velocity, U_{coflow}, to jet bulk velocity at nozzle exit, U_{jet}) of ≈0.14 and ≈0.04 respectively. The interaction between the jet and coflow in the near-to-intermediate field determines the combustion regime downstream due to the resulting gas mixtures formed. Understanding the influence of the coflow on the evolution of the jet can improve understanding of the flame stabilization mechanism and provide parametric guidelines for engineers designing combustion systems working on similar principles.

The development of a free jet may be divided between the near ($0 \leq x/D \leq 7$), intermediate, and far-field ($x/D \geq 70$). In practical systems, most of the interactive phenomenon occurs in the near-to-intermediate field ($0 \leq x/D \leq 30$) where the upstream conditions can have an influence (Ball et al. 2012). The profiles of various order statistics achieve self-similarity in the far field. Wygnanski and Fiedler (1969) made hot-wire measurements of a turbulent jet from the near to far field, providing data on mean velocities, second and third-order single-point correlations, energy balances, and length scales. The mean velocity achieved self-similarity at an earlier axial location than other turbulence statistics, and overall self-similarity of properties occurred at $x/D > 70$. Panchapakesan and Lumley (1993) measured the velocity field of a turbulent jet using hot wire anemometry and Hussein et al. (1994) did similar measurements using hot wire anemometry and laser doppler anemometry (LDA). The data was further used to evaluate transport budgets of Reynolds stress, mean kinetic energy, and turbulent kinetic energy. These are one of the many pioneering datasets on turbulent free jets that led to the characterization of this configuration. Xu and Antonia (2002) compared a jet produced from a contraction nozzle and that from a long pipe with a fully developed turbulent pipe flow, both at Reynolds number ≈86000, to study the effects of initial conditions. The contraction jet developed self-similarity faster than the pipe jet. The pipe jet had a thicker shear layer and higher turbulence intensity. This was seen to disrupt the streamwise vortex formation and pairing, which is typically associated with enhancing entrainment.

While a free jet flows into a quiescent surrounding, the presence of a turbulent coflow may influence the evolution of the turbulent jet through interactions at the interface. Several studies have also been performed on turbulent jet-in-coflow. Antonia and Bilger (1973) showed hot-wire measurements in a jet in coflow for $U_{coflow}/U_{jet} = 0.22, 0.33$. Based on the results, the authors concluded that self-similarity may not exist for this configuration and that the flow far downstream would still be affected by the initial conditions and not simply be a function of local conditions. Nickels and Perry (1996) measured the jet in coflow by hot-wire anemometry for $U_{coflow}/U_{jet} = 0.045, 0.09, 0.33$. The mean flow and stresses were further analyzed such that a similarity was drawn with a double roller vortex model. It must be noted here that in both the aforementioned studies, the free stream turbulence was kept low, 0.1%(Antonia and Bilger 1973) and 0.6%(Nickels and Perry 1996) respectively. Morton et al. (1956) introduced the theory on entrainment wherein the entrainment is directly proportional to the excess axial velocity. Gaskin and Wood (2001) presented a modification to the entrainment function to account for the jet-in-coflow as a weaker jet due to the reduction in excess velocity by allowing an ambient mean axial velocity. Or et al. (2011) measured the flow field using PIV and LIF to obtain velocity vectors and concentration fields in the first 15D of the jet to study its development under the influence of a coflow for $0.05 < U_{\text{coflow}}/U_{\text{jet}} < 0.5$. A higher coflow ratio resulted in slow decay of jet velocity and resulted in the virtual origin shifting upstream of the nozzle in several cases. The potential core length while affected to a lesser degree, was found to be shortened under a strong coflow environment. Chu et al. (1999) measured scalar concentration and velocity field in a turbulent jet-in-coflow using LIF and LDA, respectively. They obtained mean field radial profiles and instantaneous cross-sections of the jet. Uddin and Pollard (2007) provided data on the effective jet spreading rate and centreline velocity obtained by Large Eddy Simulation of a jet-in-coflow with a coflow ratio of 0.09. The data showed that the turbulence intensity distribution at the orifice does not significantly affect the virtual origin or the axial spread of the jet. The turbulence intensity of the coflow is a critical parameter that might influence the evolution of the jet in coflow system. Moeini et al. (2021) have performed a systematic study to understand the effect of low and high turbulence intensity in the coflow on the jet in the intermediate-to-far-field($45\leq x/D \leq 95$), where the turbulence intensities were 3.2 and 7% and the coflow ratios, $\text{U}_{coflow}/\text{U}_{\text{jet}}$, effectively used were between 0.058 and 0.0344. Conclusions from their results show that coflow turbulence increases jet spreading and entrainment rates; however, the relative turbulence of the coflow is very low compared to the jet at these locations($\approx$O(0.01)). Further, the variances in velocity are also seen to increase. Gaskin et al. (2004) measured the properties of a plane jet (Re = 1200) in the presence of a shallow coflow in a water tunnel. The background turbulence was varied by placing a series of submerged walls perpendicular to the direction of the flow. Higher background turbulence caused an increased rate of velocity decay. In the near field, background turbulence, at levels large enough to disrupt the jet structure, decreased dilution as the turbulent diffusion transport was less than the jet-induced entrainment. At higher turbulence levels, jet width growth reached that of jet-induced entrainment; however, the reduction in excess jet velocity due to jet structure disruption resulted in lower dilution. In the far-field, the dilution increased with background turbulence.

Researchers have studied the effect of background turbulence with zero mean flow on a jet. Khorsandi et al. (2013) studied the influence of homogeneous isotropic turbulence in the background produced by a random jet array on a turbulent jet (Re = 10600, 5800, 5300). Velocity measurements showed that background turbulence reduced the mean axial velocity and enhanced the decay rate. Further, the radial profiles of velocity are no longer self-similar. Sahebjam et al. (2022) performed PLIF measurements to observe the dispersion of a passive scalar in the same configuration (Re = 10600, 5800). The results showed a distinct behaviour when the turbulence ratio between the surroundings and the jet was greater than 0.5. This condition was achieved for the lower Re jet of 5800, wherein the downstream region, the half-width stopped growing, indicating a lack of entrainment. The shear layer was found to be preserved before the jet breakup region, as evidenced by the maintained Gaussian shape of the concentration profiles.

The entrainment of surrounding fluid in a turbulent jet is governed by the activity at the Turbulent/Non-Turbulent Interface (TNTI). This was postulated by Corrsin and Kistler (1955) and has been investigated in detail over the years. The TNTI is characterized by a marked jump in quantities such as mean axial velocity, vorticity and enstrophy from the rotational surroundings to the turbulent jet (Westerweel et al. 2009)(Chauhan et al. 2014). Entrainment can occur through either small-scale ’nibbling’ or large-scale ’engulfment’. Westerweel et al. (2009) showed that although both mechanisms occur and are responsible for mixing, ’nibbling’ is more dominant. Mistry et al. (2016), on the other hand, demonstrate that the net entrainment is scale-independent. The coherent vorticity region comprises of Large-scale Vorticity Structures (LVS) produced by the mean shear at the interface and the Intense Vorticity Structures (IVS) produced by the background turbulent fluctuations(Da Silva and Dos Reis 2011). The TNTI thickness is governed by the LVS (Da Silva and Taveira 2010) and is of the order of the Taylor microscale (λ) in turbulent jets (Westerweel et al. 2009)(da Silva et al. 2008). The TNTI is also theorized to be a thin region consisting of a Viscous Superlayer (VSL) and a Turbulent Sublayer (TSL)(Da Silva et al. 2014). The VSL is adjacent to the quiescent surroundings and governs the entrainment by viscous diffusion as evidenced by the significantly larger value of the enstrophy viscous diffusion transport over the turbulence production (vortex stretching) term, observed in DNS data (Taveira and da Silva 2014). This layer has been shown to be of a thickness $\approx 5\eta$ (Balamurugan et al. 2020). The TSL is adjacent to the turbulent core and is where the vorticity profile matching between the VSL and turbulent core occurs (Da Silva et al. 2014).

For a long time, the general consensus was that for rising background turbulence, there would be a limit beyond which an interface, consisting of a vorticity jump, would no longer exist(Da Silva et al. 2014). Kankanwadi and Buxton (2020) showed the existence of a Turbulent/Turbulent interface (TTI) through measurement in a turbulent wake with turbulent background flow. Increasing background turbulence lead to higher convolution of the interface. Unlike the TNTI, the TTI has a very low value of viscous diffusion of enstrophy compared to the inertial vorticity stretching term, indicating that, in this case, entrainment is not constrained by diffusion (Kankanwadi and Buxton 2022). Chen and Buxton (2023) show that large-scale eddy effects affect the entrainment in the near-wake and postulate that scale matching of background turbulence to wake influences the effectiveness of the turbulence on manipulating the entrainment.

Several researchers have used interface detection to determine conditional statistics to study the turbulent/non-turbulent interface of a free jet. This reduces the effect of smearing of statistics due to the spatial fluctuation of the interface in the ground frame. Westerweel et al. (2009) used laser induced fluorescence (LIF) to detect the dispersion of a dye to identify the interface by thresholding the intensity of the LIF signal obtained from this passive scalar. Conditional velocity statistics were obtained by sampling velocity vectors, obtained from PIV, with respect to this interface. Sahebjam et al. (2022) and Kohan and Gaskin (2022) similarly detected the TTI for a jet with a homogeneous turbulent surrounding with zero velocity. On the other hand, Kankanwadi and Buxton (2020) used a gradient of the LIF signal intensity and determined the edge of a turbulent wake in turbulent surroundings by identifying a contour of a given threshold value. They studied the interaction of a turbulent wake behind a cylinder with a turbulent background flow and proved the existence of the turbulent-turbulent interface (TTI). The interface can also be detected based on velocity derived criteria. Taveira and da Silva (2013) and Bisset et al. (2002) detected the interface in DNS simulations using vorticity norm as a parameter to differentiate between the irrotational, quiescent, surroundings and the rotational turbulent jet. Khashehchi et al. (2013) performed 2D2C PIV in the developing region of a free jet. They use velocity as a criteria to detect the interface such that the local velocity should be 3% of the jet exit velocity. The reasoning is that only two components of velocity are measured, hence it is better to use that as a criterion rather than a vorticity vector which would require all three components. Balamurugan et al. (2020) performed high resolution 2D2C PIV measurements of a turbulent mixing layer and used vorticity as a criteria to determine the TNTI. Watanabe et al. (2018) compared different criteria for the detection of turbulent fluids from intermittent flows, in a turbulent boundary layer. Although they use three components of the vorticity vector for detection from their DNS, they acknowledge that in the case of experiments, often, obtaining all components is difficult. Thus, they compare the 3 component vorticity magnitude, the out-of-plane vorticity magnitude, local turbulent kinetic energy, and a passive scalar as detector functions. They find that with the turbulent kinetic energy function, the isosurface of the edge is very different from the others. Further, the conditional vorticity across the interface does not have as strong of a jump in the profile.

In a jet-in-coflow, the coflow can have two effects: the first is due to the boundary layer it forms upstream over the exterior of the jet pipe, which interacts with the shear layer downstream of the nozzle exit; the second is the turbulent fluctuations in the coflow which convert the TNTI to a TTI. The aforementioned body of literature had a gap in studies with comprehensive 2D velocity measurements ranging from the near field to the intermediate field of the turbulent jet in turbulent coflow and a direct comparison to a free jet. It is especially interesting to see if this configuration, when scaled appropriately as an effective free jet, yields statistical profiles similar to those of a turbulent free jet. There is also a lack of data and analysis of velocity-based quantities conditioned to the interface between a turbulent jet and turbulent coflow, leaving much to be known on the effects of a turbulent coflow on the evolution of a turbulent jet.

The current study looks at the phenomenological effects of a turbulent coflow on a turbulent jet by varying the coflow conditions from zero velocity (free jet) to higher coflow ratios. The flow field was measured using planar PIV ranging from the near-to-intermediate field ($0 < x/D < 42$) in a non-reacting air-air jet-in-coflow. The quantities are scaled taking into account the coflow to express the jet-in-coflow as an equivalent free jet and then analyzed for any differences. These differences should originate from the presence of turbulence in the coflow and the boundary layer formed by the coflow over the jet pipe. These observations are verified and explained by analyzing conditional statistics evaluated along the interface between the jet and the surroundings. To the authors' best knowledge, this is the first study that extracts conditional velocity statistics for a turbulent jet-in-coflow entirely from PIV data. This knowledge allows us to better understand the evolution of the flow field along the axis of a turbulent-jet-in-turbulent-coflow thereby enabling a more accurate prediction of this configuration for engineering design.

2 Experiment

2.1 Experimental Setup

An experiment was set up to measure velocities in a turbulent-jet-in-turbulent-coflow by 2D2C particle imaging velocimetry (PIV), as shown in Fig 1. The jet was generated by passing compressed air through a pipe about 3 m long with an inner diameter (D) of 11 mm and a wall thickness of 0.5 mm. This ensured that the jet had a fully developed pipe flow at the nozzle exit. The flow rate was controlled by a Bronkhorst EL-FLOW massflow controller with a range of 10–500 lnpm and accuracy of ± 0.5% of reading plus ±0.1% of full scale. The coflow was produced by an open circuit low-speed wind tunnel. The jet pipe was coaxially positioned along the axis of the wind tunnel and was supported by a structure in the settling chamber and a strut closer to the exit. A wire mesh grid made of 0.5 mm diameter wires, forming square slots of 12×12 mm, was

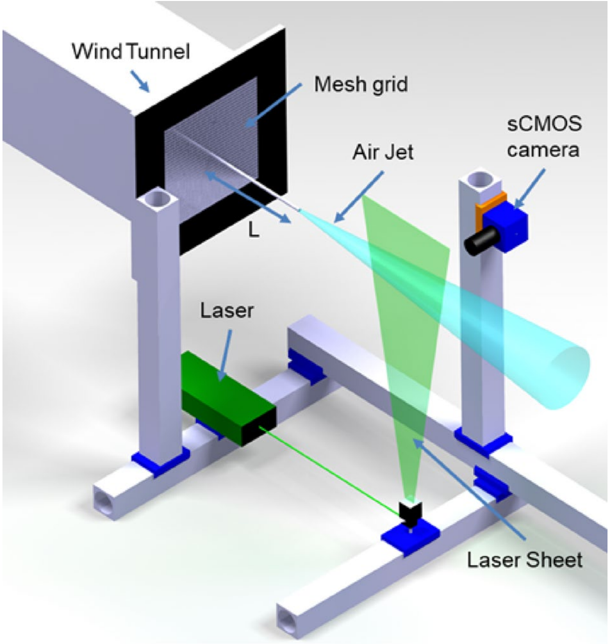

Fig. 1 Schematic of experiment

used at the tunnel exit. It served the purpose of breaking up any flow structures emanating due to the upstream support structures as well as introducing homogeneous turbulence in the coflow.

Both streams of air were seeded with particles of 1 μm diameter for PIV measurements. The coflow was seeded with a SAFEX fog generator placed near the suction side of the fan of the wind tunnel. The jet was seeded by bypassing a portion of the air through a PIVTEC aerosol generator containing DEHS oil and a manual ball valve was placed in the non-seeded branch to provide resistance to the flow to control the amount of air passing through the seeder. The PIV setup consisted of an Evergreen 200mJ laser at 532 nm and a LaVision sCMOS camera with 6.5 μm pixel size, with an acquisition frequency of 10Hz. The laser sheet was created such that a maximum of 1 mm thickness was maintained in the region of interest. The camera and laser sheet locations were shifted to image different axial sections of the jet. Measurements were done for axial locations varying from 0D to 35D, where D is the inner diameter of the nozzle, while each frame spans about 5D. The laser sheet and pipe nozzle were carefully aligned with the central axis of the wind tunnel by using a construction laser marker.

The experiments were conducted for 4 cases, one free jet (i.e., no coflow so the wind tunnel was idle) and coflow velocities of 1.9, 3.2, and 6.3 m/s, adjusted by the wind tunnel set point. During the measurements, it was ensured that the jet, coflow, and quiescent surroundings were uniformly seeded.

PIV processing was done in DaVis 8.4. Interrogation windows of 24x24 pixel with 75% overlap in the final pass were used for the PIV correlation. This results in a vector spacing, Δx, of 0.16 mm, which was maintained for $x/D<26$ and $\Delta x=0.35$ mm for $26<x/D<40$. The ratio of PIV window size to local jet halfwidth at different axial locations along the jet is always less than 0.15, indicating that the window is small compared to the characteristic length of the flow, thereby ensuring a sufficient number of vectors for analysis. The aforementioned PIV settings are tabulated in Table 1. The Kolmogorov length scale (η) is approximated as $\eta = (\frac{\nu}{\epsilon})^{0.25}$, where ν is the kinematic viscosity of the fluid and ϵ is the dissipation rate. The value of ϵ is calculated from, $\epsilon = 0.015\frac{(U_c - U_{\text{coflow}})^3}{b_u}$, where U_c is the local jet centerline velocity, b_u is the local jet half-width and U_{coflow} is the coflow velocity. This is a modified form of the correlation suggested by Panchapakesan and Lumley (1993) for a freejet. In general, the vector spacing (Δx) achieved is such that $\Delta x < 10\eta$ and beyond x/D>15, $\Delta x < 6\eta$. The detailed conditional statistics are analyzed in the region 20<x/D<25 where $\Delta x \leq 3\eta$.

2.2 Flow Conditions

We investigated different coflow velocity conditions while keeping a constant jet exit bulk velocity, U_{jet}=20 m/s, by maintaining a constant mass flow rate of air using the flow controller. This ensured that the jet Reynolds number based on bulk velocity and nozzle diameter remained constant (Re = 14000), between different cases. The cases were characterized using the concept of momentum radius (θ_{coflow}), which may be defined as the equivalent radius required of a stream flowing at the velocity of the coflow to have the same momentum as the jet. Thus, for lower coflow velocity, a larger radius is required. It is defined as:

$$\begin{aligned} \theta_{\text{coflow}} &= \sqrt{\frac{J_0}{\pi \rho U_{\text{coflow}}^2}}, \\ J_0 &= \frac{\pi}{4} D^2 \rho_0 U_{\text{jet}}^2, \end{aligned} \tag{1}$$

where U_{coflow} is the coflow velocity, U_{jet} is the bulk jet exit velocity, D is the nozzle diameter, and J_0 is the source momentum flux. This definition has been used in the literature on free jets. Dahm and Dibble (1988) define a ratio x/θ_{coflow}, where x is the distance along the jet axis, such that for values of $x/\theta_{\text{coflow}} \leq 2$ the flow can be considered to be negligibly affected by the coflow and hence be treated as a free turbulent jet. Thus, a higher coflow ratio results in an earlier transition to an effective jet-in-coflow along the jet axis, listed as x/D_{trans} in Table 2. It should be noted that this threshold is an approximation as is seen in the case of Ganapathisubramani et al. (2007) where at x/D=32 a value of $x/\theta_{\text{coflow}} = 3$ was still considered a free jet.

The coflow forms a boundary layer over the exterior of the central jet pipe. This is characterised by extracting the axial velocity profile at the first station closest to the nozzle exit from the PIV data. As this is not measured over the wall of the pipe but downstream where the wall just ends, the velocity measured does not achieve an absolute zero value. However, for the sake of characterization, all the coflow conditions are measured in the same way, hence a good comparison can be obtained. The boundary layer properties(displacement thickness(δ^*), momentum thickness(θ) and shape factor(H)), tabulated in Table 2, are calculated by fitting a cubic spline to the measured points and extrapolating it to the point where zero velocity is achieved, as shown in Fig 2. The Reynolds number based on momentum-thickness (Re_θ), tabulated in Table 2, increases with increasing coflow ratio.

The turbulence level of the coflow is also expected to influence the evolution of the flow field. Turbulence in the coflow was enhanced by a grid composed of cylindrical elements. For the given set of coflow conditions, the Re_d, where d is the diameter of the rod of the mesh grid on the coflow outlet, ranges from 63 to 210, as listed in Table 2. As mentioned by Roshko (1954), vortex shedding for a cylinder is stable and laminar for $40 < Re < 150$

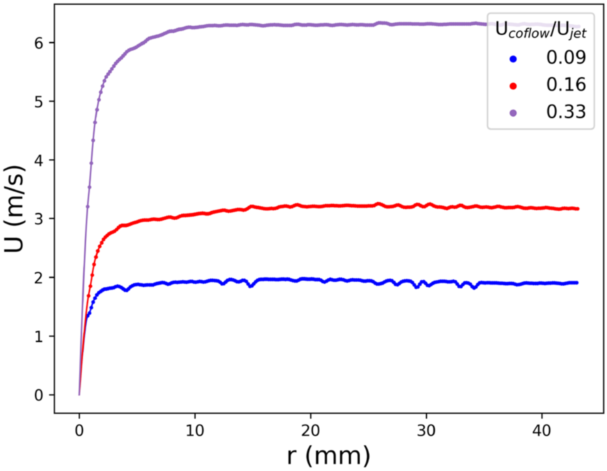

Fig. 2 Boundary Layer profile around pipe extracted from PIV measurements

and transitions to turbulent between $150 < Re < 300$. Thus, in the current study, there is vortex shedding under both stable and transitioning regimes depending on the case. According to the design recommendation of Vita et al. (2018), after a distance $x/M > 10$, where M is the spacing between adjacent grid elements, well-developed turbulence behind a grid is obtained where the statistics are driven by dissipation and the turbulence intensity decays as a power law. However, a distance of the order of x/M=50–100 is required to achieve acceptable homogeneity and isotropy(Kurian and Fransson 2009). Thus, a trade-off is made to achieve a significant level of turbulence intensity in the region of interest and the distance of the pipe exit from the grid plane, L, is set such that L > 120 mm (shown in Fig 1).

The turbulence intensities of the coflow in the current study are shown in Fig 3, and the total magnitude is between 3–4%, with a slight decrease with coflow ratio. However, when the velocity fluctuations are scaled by the jet excess velocity (U_c-U_{coflow}), as shown in Fig 4, there is a clear increase in turbulence intensity with coflow ratio. This indicates that the jet perceives the coflow fluctuations as effectively increasing with coflow velocity.

2.3 Interface detection

The interface is defined as a thin region separating the high turbulence region (jet interior) from the low turbulence region (surrounding coflow). For a turbulent free jet, this has been shown through DNS studies to be well represented by a surface of thresholded vorticity or a passive scalar (Bisset et al. 2002)(Da Silva and Taveira 2010)(Watanabe et al. 2015). In most experimental studies, interface detection is done by introducing a dye (as a scalar) in one of the streams and the interface is said to be located at a certain defined dye concentration limit as detected by PLIF (Westerweel et al. 2009)(Kankanwadi and Buxton 2020)(Mistry et al. 2016)(Chauhan et al. 2014). In this work, interface detection is done purely through the vector field due to the high resolution as also done by Balamurugan et al. (2020). The criterion used for detection is vorticity magnitude ($|\Omega|$) based on the assumption that it is higher within the turbulent jet than in the turbulent coflow and quiescent surroundings. The quantity is calculated for an instantaneous vector field, where the

Fig. 3 Velocity RMS vs Coflow ratio scaled to coflow velocity

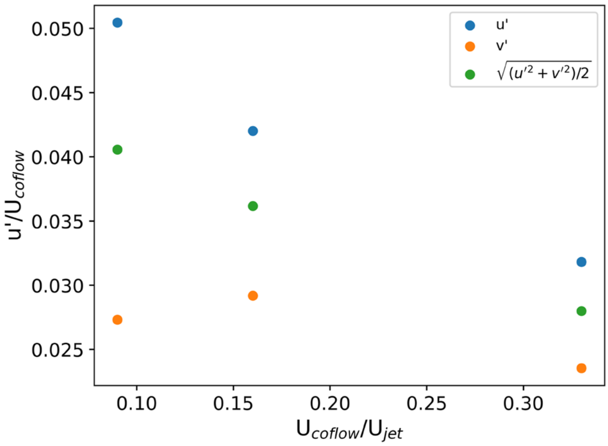

Fig. 4 Velocity RMS vs Coflow ratio scaled to relative jet velocity

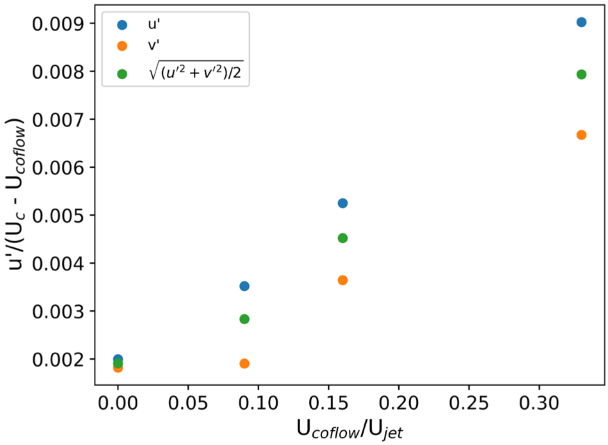

gradients are evaluated after processing with a 2D Savitsky-Golay filter with a window size of 5x5 and a 2^{nd} order polynomial of the form:

$$z = a_0 + a_1x + a_2y + a_3xy + a_4x^2 + a_5y^2 \tag{2}$$

, where x and y are the distances with respect to the center point of the window. Thus, the filtered value of 'z' is a_0 at x=y=0, and the derivatives with respect to x and y are the coefficients a_1 and a_2, respectively. This filter provides the advantage of noise reduction while retaining the relevant flow features. A detailed analysis of the sensitivity to window size is derived by Elsinga et al. (2010), where it is shown that spatial frequency response of the PIV cross-correlation and Savitsky-Golay regression are similar and, therefore, the noise reduction does not lead to spatial resolution loss. Finally, the value is normalized as $\Omega^* = |\Omega| y_{1/2}(x)/(U_c(x))$, where $y_{1/2}(x)$ is the jet half-width and $U_c(x)$ is the axial velocity at the centerline at a given x distance from the nozzle. This is done locally, by taking the normalization values from the unconditioned average for each axial location.

Table 1 PIV experiment conditions

Field of view	100 mm
Laser sheet thickness	1 mm
dt	1 μ s
Pixel size	6.5 μ m
Interrogation window size in final pass	24x24 pixel
Window overlap in final pass	75%
Vector spacing (mm)	0.16 (x/D<26), 0.35 (26<x/D<40)

A threshold value for the normalized vorticity (Ω^*_{thresh}) is used to distinguish the region within the jet from the surroundings which is determined using a method similar to Balamurugan et al. (2020), which in turn is based on threshold determination methods proposed by Mistry et al. (2016) and Prasad and Sreenivasan (1989). As the surroundings have a low/moderate level of turbulence, the higher level of vorticity within the jet should be distinguishable. This is done by plotting the area in the image (A_{jet}, in pixels) above a certain threshold, which is effectively the area within the turbulent jet, against varying threshold values (Ω^*_{thresh}). This results in a monotonically decreasing curve, shown in Fig 6a that finally reaches a constant value. The derivative of this curve is taken, where there is an initial rising part, and it ends with a nearly zero value. Two lines are fit to these regions (Fig 6a), and their intersection location is used as the threshold value. Applying this thresholding process results in several disjointed regions, as can be seen by the vorticity contours in Fig 6b; however, to obtain a continuous interface, the most intense vorticity regions need to be clustered together.

The density based spatial clustering for applications with noise (DBSCAN) (Schubert et al. 2017) algorithm is applied to the thresholded data to determine clusters. It is an image-processing algorithm that clusters closely spaced points and marks outliers that lie separated in low-density regions as noise. The algorithm takes two input parameters, epsilon, which is the distance of search from a point for neighbors, and Minpts, which is the minimum number of points that should lie within a radius of epsilon from a point to classify it as a core point. The value of epsilon and Minpts were fixed to 3 and 20, respectively. The values were selected based on a manual sensitivity analysis. The values imply that within a radial distance of epsilon=3 pixels at least Minpts=20 pixels should be found in the thresholded image for the point to be considered to be part of a cluster. This means that in a 7x7 pixel square (area=49 pixels), 20 pixels should be found, i.e ~41% filled. This was found to provide a good balance between identifying filled points and leaving enough distance to exclude islands/ noise points. Small variations of these values did not impact the edge detection significantly. This results in the detection of the most intense vorticity structures. The clustering algorithm is applied in the following steps:

1. DBSCAN algorithm is applied on the thresholded image such that only pixels above a threshold are considered for the clustering process.
2. The largest cluster is chosen
3. Image is binarized by setting the value of the pixels of the largest cluster to 10 and the remaining pixels to -10.

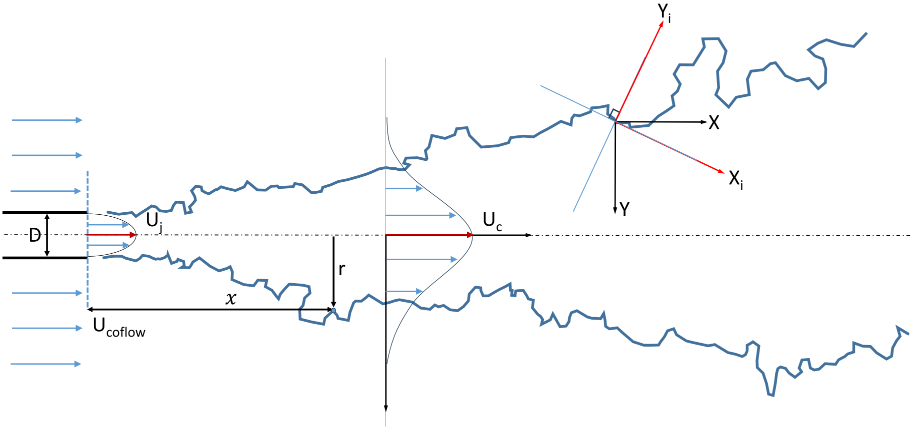

Fig. 5 Representative sketch of the flow configuration. X$_i$, Y$_i$ is the transformed coordinate system in the frame of the local interface

Table 2 Coflow conditions of operation

U$_{coflow}$(m/s)	U$_{jet}$(m/s)	U$_{coflow}$/U$_{jet}$	x/D_{trans}	Re_d	δ^*(mm)	θ(mm)	Re$_\theta$	H
0	20	0	∞	0	–	–	–	–
1.9	20	0.09	10	63	2.55	1.78	235	1.43
3.2	20	0.16	5.5	107	4.48	3.2	693	1.40
6.3	20	0.33	3	210	2.93	1.82	769	1.61

4. The binarized image is inverted such that the largest cluster pixels now have a value of -10

The first clustering step is applied to the image thresholded by the value of $|\Omega| y_{1/2}(x)/(U_{\mathrm{c}}(x))$ obtained from the area method, resulting in an image such as Fig 6c. The clustering algorithm is applied a second time on the resulting image thresholded by zero, such that only pixels with positive values are considered. This results in an image such as Fig 6d. Finally, the interface is identified as the edge of the region with a positive value, using contour detection in OpenCV (Bradski 2000), which is overlayed on the vorticity field in Fig 6b and on the axial velocity contour in Fig 6e.

Statistics are collected in a relative coordinate frame oriented perpendicular to the local edge. The slope of the edge is obtained by fitting a 3^{rd} order polynomial in a region of 5 edge points around the point of interest. The velocity in the conditional frame is obtained by projecting the ground frame velocity vector in the rotated coordinate system. Thus, the "axial component" in the rotated frame is parallel to the interface and the "radial component" is perpendicular to the interface as shown in Fig 5.

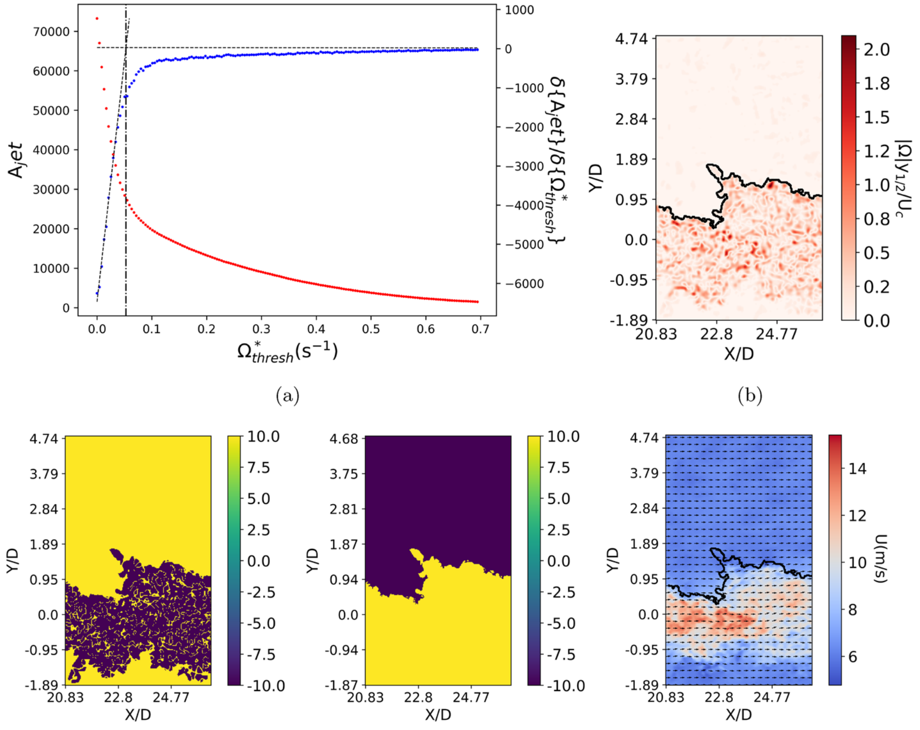

(a)

(b)

(c)

(d)

(e)

Fig. 6 Interface detection methodology demonstrated on an instantaneous image of $U_{\mathrm{coflow}}/U_{\mathrm{jet}}=0.33$ **a** Area method demonstrated by the area detected within the turbulent jet, A_{jet} (red points), for varying threshold values (Ω^*_{thresh}) and the corresponding derivative curve (blue points). **b** Instantaneous interface overlayed on vorticity contour. **c** First DBSCAN clustering. **d** Second DBSCAN clustering. **e** Instantaneous interface overlayed on axial velocity contour along with velocity vectors

3 Results

3.1 Mean field

The jet was imaged at different axial locations in the near and intermediate field (up to $x/D = 42$). We first explore the overall evolution by tabulating the average axial velocity field in Fig 7. The images are presented as U/U_j, where U_j is the velocity at the centerline at the jet exit, which is kept constant across all cases of varying coflow. Thus, it can be seen that cases with a higher coflow ratio have a higher coflow velocity. At first glance, it seems that the free jet decays faster in the streamwise direction and has a larger width compared to cases with higher coflow.

The turbulence intensity distribution is shown in Fig 8. The qualitative evolution is as expected, where high turbulent fluctuations originate in the shear layers starting close to the nozzle exit and the region of turbulent fluctuations expands radially as the jet evolves further downstream. The turbulence intensity is higher further downstream in all cases, due to mean axial velocity decay at a rate that is faster than turbulence

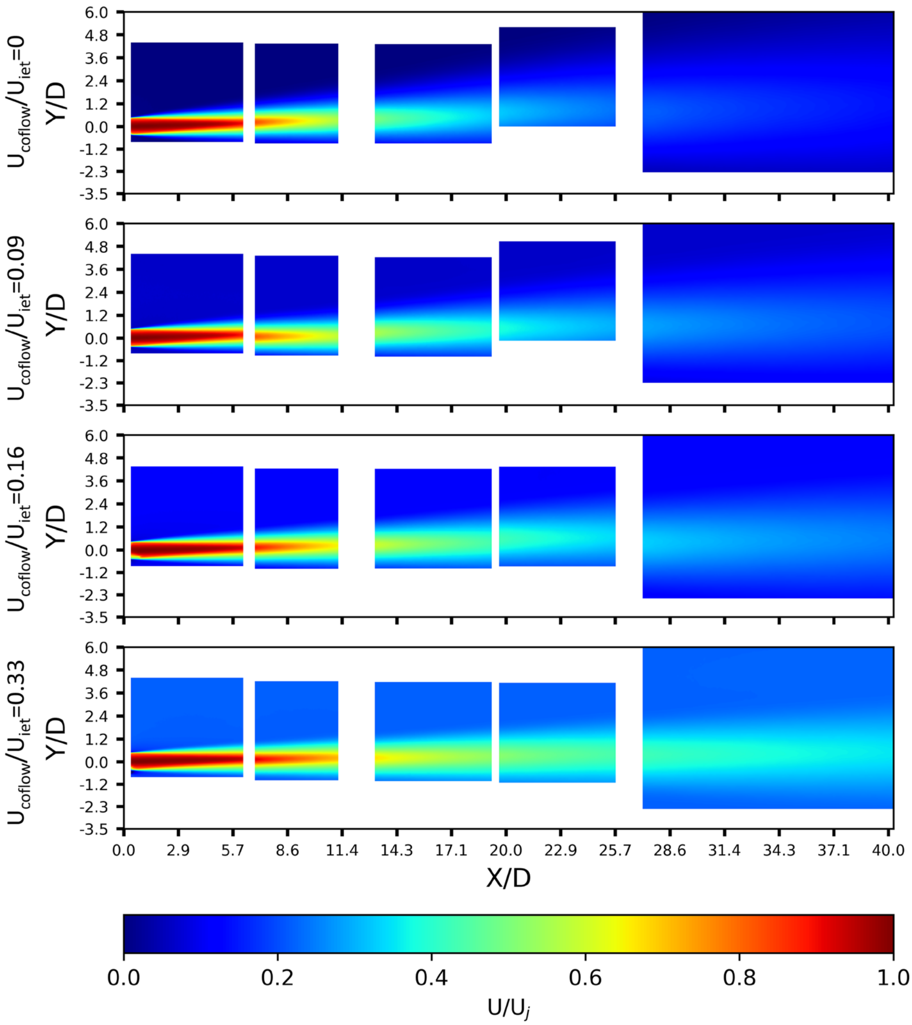

Fig. 7 Axial velocity distribution over the measured domain, compared across cases of varying coflow ratio

fluctuation dissipation along the axis. Also, it can be seen that an increase in the coflow ratio results in a higher turbulence intensity, especially for $19.6 < x/D < 40$.

The jet centerline axial mean velocity is shown in Fig 9a. In the self-similar region, the axial velocity decays as

$$\frac{U_j}{U_c(x)} = \frac{1}{b}(\frac{x}{D} - \frac{x_0}{D}) \tag{3}$$

where $U_c(x)$ is the jet centerline velocity at axial location x, b is the decay constant and x_0 is the virtual origin. Typically, this linear fit is done for $x/D > 15$. The velocity decays along the axis, as is expected for a round turbulent jet, where the value of $b = 5.30$ (Table 3), which is comparable to 5.6 from Xu and Antonia (2002). One can notice that the decay line

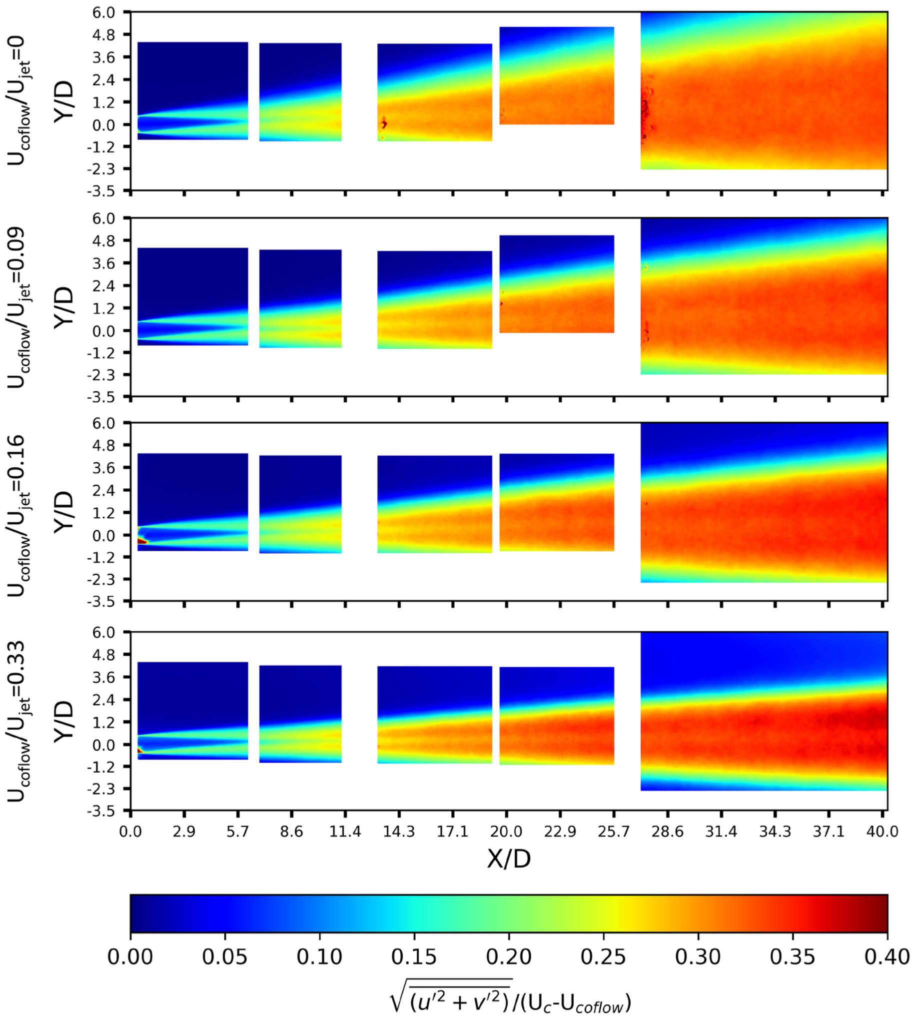

Fig. 8 Turbulence intensity distribution over the measured domain, compared across cases of varying coflow ratio

deviates from a linear fit as the coflow ratio increases. To correct this and represent the case as a free jet relative to the coflow, appropriate scaling of $\frac{U_j-U_{coflow}(x)}{U_c(x)-U_{coflow}(x)}$ is applied, where $U_{coflow}(x)$ is the coflow axial velocity at that axial location. This results in scaled decay constant and virtual origin represented as b^* and x_0^*, respectively. The scaled jet decay profiles are re-linearized as seen in Fig 9b; however, the slopes are still different, as listed in Table 3. The maximum value of the decay constant, b, is 21.21 and after scaling b^* is 6.59 for the highest coflow case. The virtual origin location, x_0/D is negative for non-zero coflow, indicating a location behind the nozzle exit, and after scaling, x_0^*/D= 3.16 for the free jet and reduces to 2.06 for the case with the highest coflow. In comparison, Xu and Antonia (2002) obtained a value of 3.7 for a free jet. It must be noted that cases with a higher coflow ratio have higher turbulence when scaled with the relative velocity of the jet

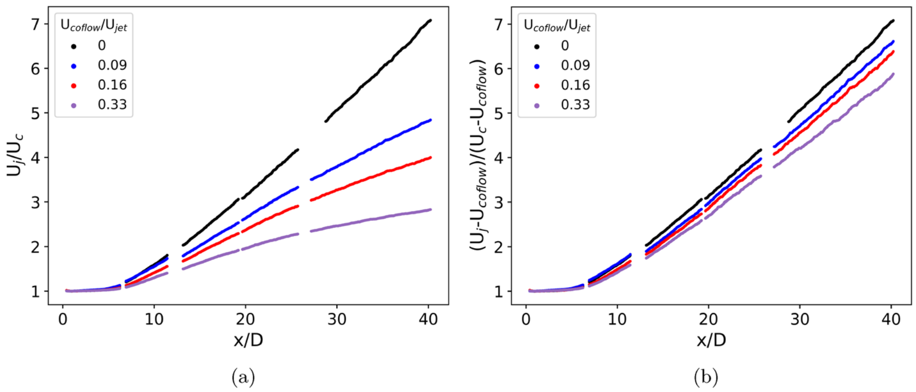

Fig. 9 Jet centerline velocity decay expressed as (a) U_j/U_c (b) $(U_j-U_{coflow})/(U_c-U_{coflow})$

to the coflow, which seems to influence the velocity decay rate. Further, the establishment of linearity with scaling shows its importance to correctly represent the jet in coflow as a 'slower moving jet' in the frame of reference of the coflow and comparing it to a free jet.

The evolution of the half-width, $y_{1/2}$, is shown in Fig 10, where the half-width for a free jet is defined as the distance from the centerline to the radial location where the axial velocity is half that of the local centerline axial velocity. The mean spread rate (A) of $y_{1/2}$ beyond x/D>15 is given by

$$\frac{y_{1/2}}{D} = A\frac{x}{D} - B \tag{4}$$

For a turbulent-jet-in-turbulent-coflow, the point is redefined to be along the radial direction where the axial velocity is the average of the maximum and coflow velocity at that axial station. The halfwidth remains approximately constant, with a slight decay, in the first 5D but then increases further downstream. The halfwidth of the free jet has a higher mean spread rate than the cases with a higher coflow ratio, which is also tabulated in Table 3. The decay constant, A, is 0.089 for the free jet and drops to 0.037 for the case with the

Fig. 10 Jet half width ($y_{1/2}$) v/s x/D

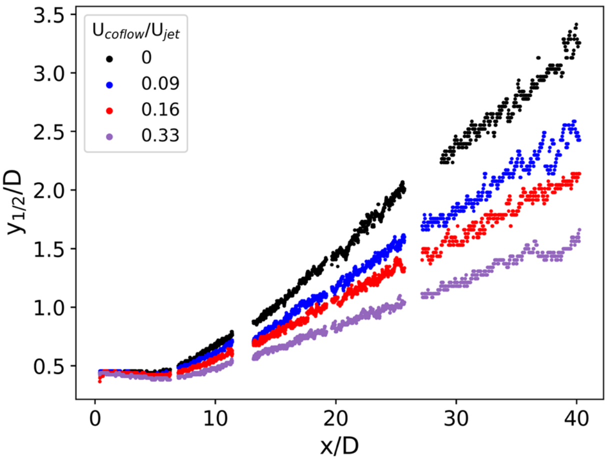

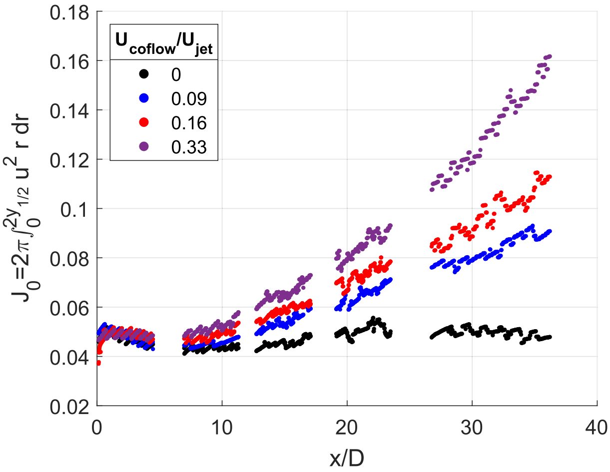

Fig. 11 Jet momentum (J_0) v/s x/D

Table 3 Jet halfwidth and spreading characteristics

$\frac{U_{\text{coflow}}}{U_{\text{jet}}}$	b	b^*	x_0/D	x_0^*/D	A	B
0	5.30	5.30	3.16	3.16	0.089	0.307
0.09	8.88	5.70	-3.50	2.92	0.066	0.127
0.16	11.81	5.92	-8.12	2.87	0.054	0.017
0.33	21.21	6.59	-21.62	2.06	0.037	-0.092

highest coflow. In comparison, Xu and Antonia (2002) obtained a value of 0.086 for a free jet.

Fig 11 shows jet momentum flux ($J_0 = 2\pi\int_0^{2y_{1/2}} u^2 r dr$) variation along the axis. It is calculated by integrating momentum flux from the jet centerline to a radial distance twice that of the jet halfwidth. In 0<x/D<5, all 4 cases of coflow ratio have almost the same momentum, which should also be the case as the same mass flow rate of the jet was maintained. As we go further downstream, the free jet maintains this level of momentum, while for increasing coflow values, the momentum increases in the downstream direction. This is caused by the additional momentum present in the coflow which is entrained by the jet.

3.2 Radial Profiles

Radial profiles are presented at various axial distances from the jet nozzle. The radial distance is represented as a ratio of distance (r) to the local jet half width ($y_{1/2}$). The data is normalized as $\frac{U(x)-U_{coflow}(x)}{U_c(x)-U_{coflow}(x)}$ relative to the coflow such that a jet-in-coflow would represent a "slower moving" turbulent jet in a zero mean velocity, turbulent environment. This results in a value of 1 at the jet centerline and 0 in the coflow for all cases. A similar normalization has been used by Zhang and Chin (2020) where they analyzed cases for $U_{\text{coflow}}/U_{\text{jet}}$= 0, 0.0833, 0.166, and 0.333. Other works such as that by Nickels and Perry (1996) and Antonia and Bilger (1973) also scale their data similarly. Ideally, the scaled profiles from different cases would overlap; however, the presence of a boundary layer generated by the coflow over the jet pipe and the turbulence of the coflow can lead to some differences.

The mean axial velocity profiles are shown in Fig 12 at x/D = 5, 10, 22 and 30, for 4 different conditions of coflow velocity ratio, $U_{\text{coflow}}/U_{\text{jet}} = 0, 0.09, 0.16$ and 0.33. The profiles show a significant overlap between the different cases; however, a difference is seen at the interface between the jet and coflow ($r/y_{1/2} = 2$), in the form of a separation of profiles for the different coflow ratios. For cases with higher coflow ratios, the profile decreases faster in the radial direction leading to region of "velocity deficit" compared to the free jet.

The normalized axial turbulence fluctuation profiles are plotted in Fig 13 at x/D= 5, 10, 22, 30. The profiles have an 'M' shape with turbulence intensity peaks around $r/y_{1/2}=\pm$ 0.5. There is an intersection between the profiles of the free jet and coflowing jets located between $\text{r/y}_{1/2}$ ≈1.8 and $r/y_{1/2}$ ≈2.5, which also corresponds to the inflection point of the profiles. At x/D=5 cases with lower coflow have a higher relative turbulence intensity ($\Delta \approx 0.025$) at the centerline but this difference reduces further downstream to nearly zero. In the radial vicinity of the inflection point ($r/y_{1/2}$ ≈1.8), the coflowing jets have a higher value towards the centerline whereas in $2.25< r/y_{1/2} <3$, the free jet has a higher turbulence intensity. At x/D=22 and 30, the trend is similar but the higher turbulence intensity of free jet is up to $r/y_{1/2}$=2.5 beyond which it starts dropping under the highest coflow ratio cases. This shows that there is a higher turbulence region for the free jet compared to

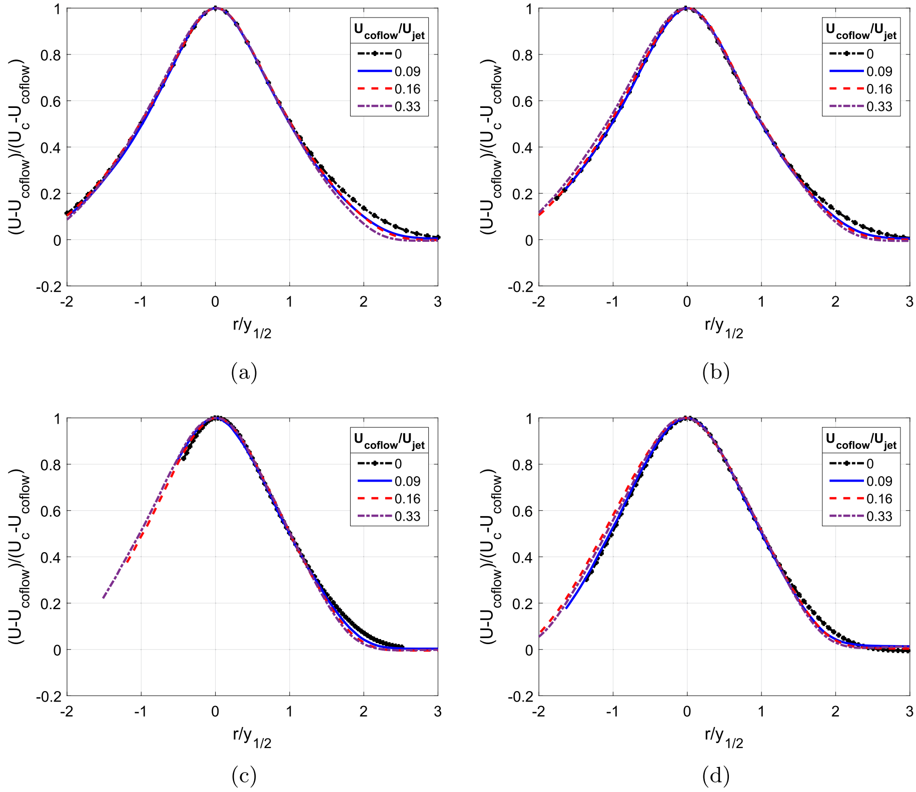

(a)

(b)

(c)

(d)

Fig. 12 Axial velocity profile at (a) x/D=5, (b) x/D=10, (c) x/D=22, (d) x/D = 30

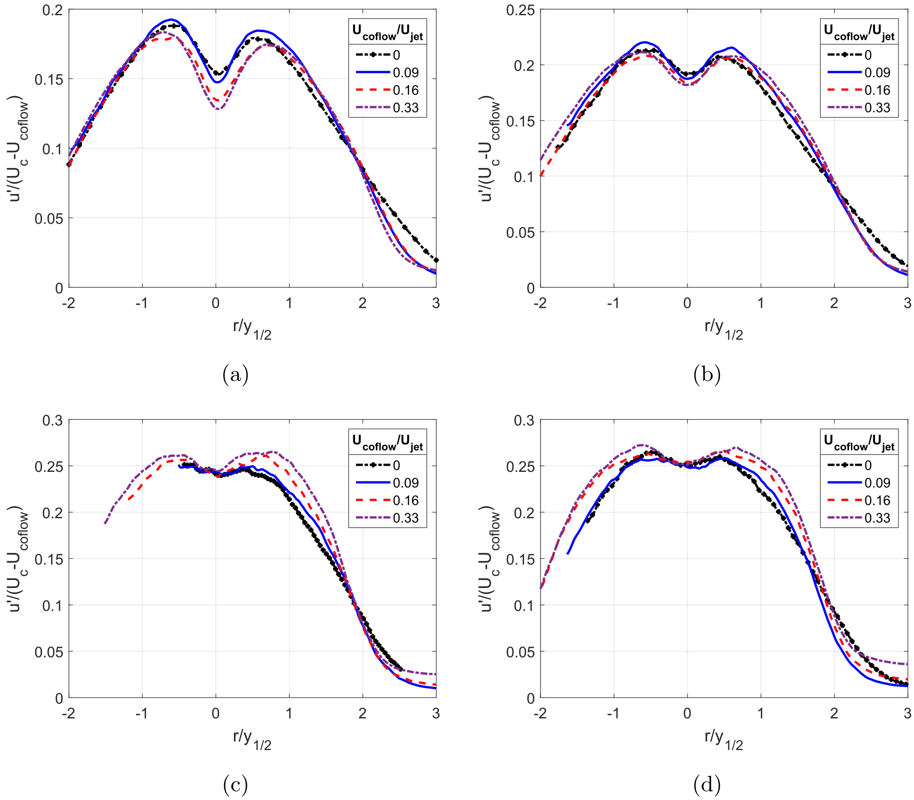

(a) (b) (c) (d)

Fig. 13 Axial turbulence intensity profile at **a** *x*/*D*=5, **b** *x*/*D*=10, **c** *x*/*D*=22, **d** *x*/*D*=30

a turbulent-jet-in-turbulent-coflow, which is located between the inflection point and the far surroundings. This indicates a higher propagation of turbulence from the turbulent jet to the surroundings in the case of a free jet than that of a jet-in-coflow. This is supported by higher entrainment rates for a free jet seen through faster centerline velocity decay and larger half-width seen in Sect. 3.1. Also, there is a higher turbulence intensity peak as the coflow ratio increases.

The normalized Reynolds shear stress (RSS) profiles, shown in Fig 14, indicate momentum transport due to turbulence. It achieves a peak in a region, $0.7< r/y_{1/2} <1.0$, between the turbulent jet and the turbulent coflow, and has a value of zero in the surrounding far field. The peak shifts radially outward for higher coflow ratios.

The one-point statistics reveal that the higher coflow cases exhibit a deficit in the mean axial velocity profile near the interface region with respect to the free jet. Furthermore, the turbulence intensity and Reynolds Shear Stress reach higher peak values compared to a free jet at x/D=22 and 30. The velocity deficit identified in the axial velocity profiles is caused by the boundary layer over the external wall of the pipe that produces the central jet. The wake originating from this boundary layer shields the jet from the coflow, thereby reducing the amount of turbulent interaction and retaining a large velocity gradient at the interface as far as x/D=30. This shielding also dampens the turbulence exchange due to which the jet and coflow sides retain their respective turbulence intensity levels. As the coflow

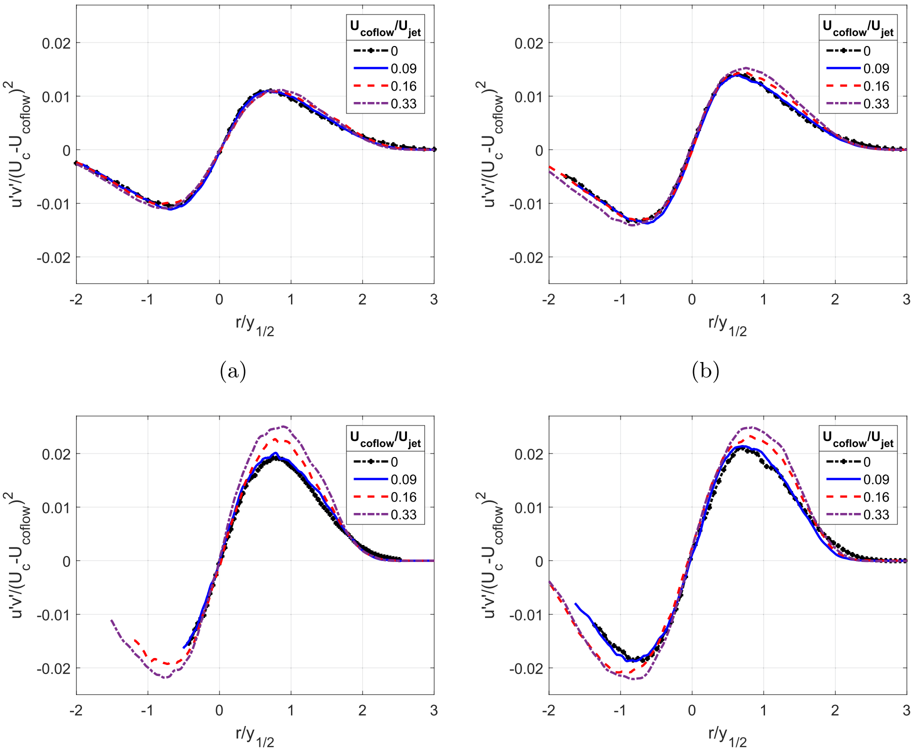

(a) (b)

(c) (d)

Fig. 14 Reynolds shear stress profile at **a** *x*/*D*=5, **b** *x*/*D*=10, **c** *x*/*D*=22, **d** *x*/*D*=30

has a low turbulence intensity, this is not sufficient to disrupt the interface and enhance entrainment as was observed in higher background turbulence cases (Sahebjam et al. 2022) (Gaskin et al. 2004). This leads to a larger radial gradient in the turbulence intensity profile for higher coflow velocity.

3.3 Conditional Statistics Along the Interface

Mean field statistics, when observed from the ground frame of reference, may lead to the smearing of gradients. Conditional statistics are assembled by sampling data at fixed locations with respect to the local interface. Therefore, they provide more accurate information about phenomena near the interface. The interface is detected using the methodology explained in Sect. 2.3. Conditional statistics are assembled by sampling points along a line perpendicular to the local interface. The slope of the tangent is determined by fitting a 3rd order polynomial in a region of 5 points along the detected interface around the point of interest. The points along the perpendicular are equispaced and the velocity data at these points are obtained by bilinear interpolation of the underlying original PIV data. Finally, the vectors are projected onto the rotated local frame of reference of the interface such that the conditional axial velocity is tangent to the interface and conditional radial velocity is perpendicular to the interface. The conditional data is presented in Fig 15 where

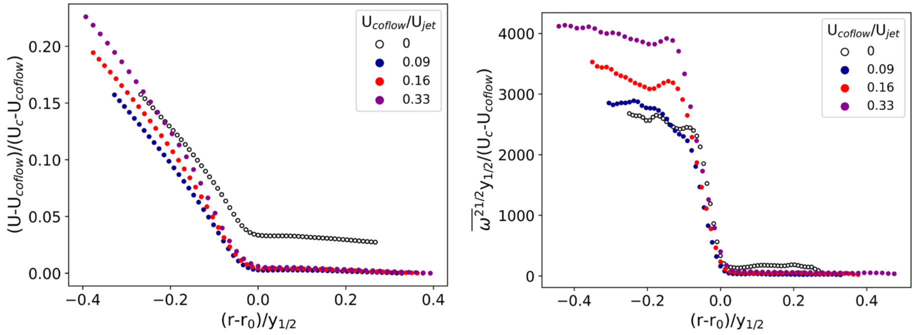

(a) Conditional axial velocity

(b) Conditional enstrophy

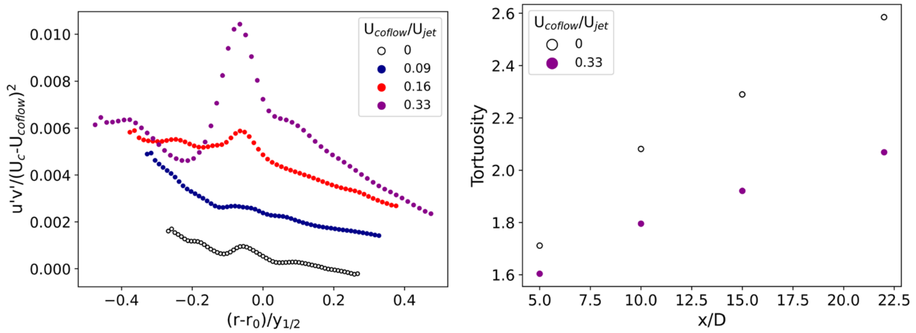

(c) Conditional Reynolds Shear Stress

(d) Tortuosity

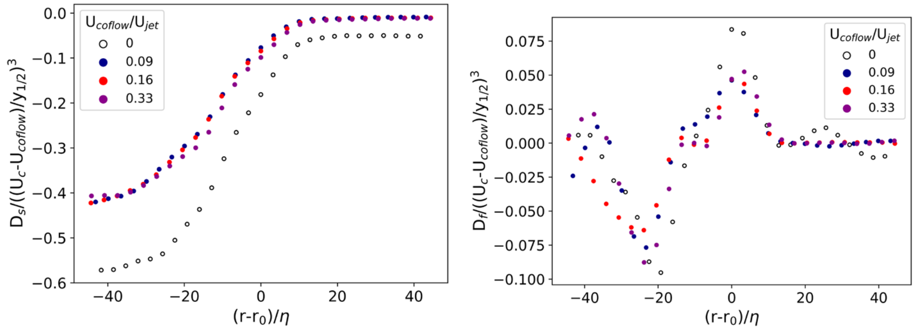

(e) Enstrophy Dissipation (D_s)

(f) Enstrophy Diffusion (D_f)

Fig. 15 Conditional radial profiles at x/D=22 (**a**, **b**, **c**, **e**, **f**). Tortuosity variation along the jet axis (**d**)

the turbulent jet interior is at the negative x-axis location and the coflow/surroundings are located at the positive x-axis locations. To improve statistical conversion, samples are collected over a window, 20 vectors wide, along the frame centered at the point of interest on the interface.

The conditional axial velocity, shown in Fig 15a, shows that the cases with coflow have a visible velocity deficit close to the interface compared to the free jet. However, the profiles of the three cases with coflow collapse over each other and deviate towards the centerline. The deficit region clearly shows the influence of the boundary layer, originally generated over the external surface of the jet pipe by the coflow, in the vicinity of the interface, creating a larger velocity jump across the interface than a free turbulent jet (U_{coflow} /U_{jet}=0).

Enstrophy is an indicator of small-scale turbulence activity, and there is a strong jump of enstrophy across the interface of a free jet (Westerweel et al. 2009). The conditional enstrophy profile in Fig. 15b captures this jump across the interface, validating the interface detection based on vorticity. While the profiles collapse over each other in the coflow region, the cases of higher coflow show a higher enstrophy within the jet. This shows a higher level of small-scale turbulence. Evidence of large-scale turbulent activity is seen in Fig. 15c, through a higher peak for a higher coflow ratio, around the interface. This also corresponds well with higher peaks seen in the mean RSS radial profiles in Sect. 3.2.

The turbulent interface is highly convoluted. This would cause a spatial variation of the collection point for the conditional statistics. Thus, quantifying the degree of convolution would give an objective parameter to help appreciate the significance of conditional statistics and also differentiate between an interface formed in a free jet and that of a turbulent-jet-in-turbulent-coflow. Tortuosity is a parameter used to quantify the level of contortion of a surface. In this work, the tortuosity of the interface is defined as the ratio of the length of the curve to the shortest distance between the two extreme ends, similar to that by Kankanwadi and Buxton (2020). The tortuosity, as shown in Fig. 15d, of the interface along the axial stations increases in the downstream direction. It is also lower in magnitude for higher coflow velocity.

The viscous super layer (VSL) is known to be a feature of the TNTI where viscous diffusion dominates over the production of enstrophy(Corrsin and Kistler 1955)(Da Silva et al. 2014). The enstrophy transport equation is expressed as

$$\frac{D}{Dt}\left(\frac{1}{2}\omega_i\omega_i\right) = \underbrace{\omega_i\omega_j S_{ij}}_{\text{Production}} + \underbrace{\nu\frac{\partial^2}{\partial x_j \partial x_j}\left(\frac{1}{2}\omega_i\omega_i\right)}_{\text{Diffusion}} \underbrace{-\nu\frac{\partial \omega_i}{\partial x_j}\frac{\partial \omega_i}{\partial x_j}}_{\text{Dissipation}} \tag{5}$$

As 2D data is available in the current experiment, only the out-of-plane component of vorticity ($\omega_z(x,y)$) can be evaluated. Therefore, the 2D surrogates of dissipation($D_s = -\nu\frac{\partial\omega_z}{\partial x}\frac{\partial\omega_z}{\partial y}$) and diffusion($D_f = \nu[\frac{\partial^2}{\partial^2 x}(\frac{1}{2}\omega_z\omega_z) + \frac{\partial^2}{\partial^2 y}(\frac{1}{2}\omega_z\omega_z)]$) can be obtained and the production term cannot be evaluated. The diffusion term in Fig. 15f shows a positive peak, where the VSL is located at the interface and has a peak-width of $\approx 10\eta$. Given that the vector spacing is $\approx 3\eta$ in this region and the VSL for a TNTI is shown to be $\approx 5\eta$ in previous works(Da Silva et al. 2014)(Balamurugan et al. 2020), the structure of the VSL may not be fully resolved, however, the extents should be fairly captured. The dissipation term in Fig. 15e indicates higher diffusion towards the jet centerline and reduced magnitude of dissipation for cases with coflow. Further interpretation of these terms and their impact are discussed in Sect. 4. Kankanwadi and Buxton (2022) found that for a TTI with high outer turbulence (greater than levels achieved in this study), the vorticity stretching term, i.e. the production term in Eqn 5, takes precedence. Also, as vorticity stretching need not be constrained to be zero as is in a TNTI, it facilitates a mechanism of enstrophy production throughout the entire thickness of the TTI. However, the viscous diffusion and dissipation terms still exist with a similar magnitude for both low and high outer turbulence. This is postulated to be a remnant of the VSL, but the magnitude is lower than the vortex stretching term for most of the VSL. This questions the physical significance of scaling the TTI thickness by the Kolmogorov scale. In our results, the magnitude of vortex stretching cannot be checked as the results are from planar PIV, so in plane vorticity components cannot be obtained.

4 Discussion

The coflow can influence the evolution of the turbulent jet through the boundary layer it generates over the jet pipe and the turbulence in coflow. Increasing U_{coflow}/U_{jet} leads to larger values of b^*, thereby showing slower jet centerline velocity decay. Also, the half-width is seen to be smaller at the same axial location. This indicates that entrainment from the surroundings is reduced, and this is also supported by the conditional radial velocity profile, which shows a significantly lower magnitude at the interface than the free jet condition. Upon correct scaling, if the equivalent free jet have a Reynolds number such that they have achieved the mixing transition (Dimotakis 2000), the centerline decay profiles in Fig. 9b should collapse on each other for all coflow ratio cases. As this is not the case, this is directly attributed to the "shielding" effect of the boundary layer developed by the coflow around the jet, which reduces turbulent exchange between the two streams. It must be noted that the entrainment and profiles mentioned above are for the scaled jet, i.e., in a normalized form that makes them comparable. According to the entertainment theory (Morton et al. 1956), the entrainment rate is proportional to the centerline velocity. However, this would be an absolute entrainment that varies even between two free turbulent jets of the same Reynolds numbers but with different diameters and, hence, jet centerline velocities.

In the conditional enstrophy transport equation, the diffusion term (D_f) peak width at the interface, which indicates the VSL structure, remains unchanged for varying coflow ratios, which shows that the low turbulence intensity level of the coflow does not influence the interface structure. However, the boundary layer generated by the coflow over the jet pipe, creates a shielding effect, indicated by a local velocity deficit. This correlates with lower magnitude of enstrophy dissipation (D_s) in the jet core, leading to higher enstrophy and RSS peaks on the jet side of the interface for $U_{coflow}/U_{jet} > 0$. This "shielding effect" is the reason why the scaled trends of the jet-centerline decay and half-width do not collapse on the curves of the free turbulent jet and, in fact, indicate lower relative entrainment.

Higher turbulence intensity in the background has been observed to increase the tortuosity/contortion of the interface (Kankanwadi and Buxton 2020)(Sahebjam et al. 2022); however, in this study, as the turbulence intensities are too low (<6%), they are unable to influence the interface shape. Thus, the "shielding effect" prevents intense contortion of the interface, leading to lower tortuosity in the jet-in-coflow than in a free jet.

5 Conclusion

This work aims to study the evolution of a jet-in-coflow in the near-to-intermediate field (NIF) in the presence of low turbulence intensity (<6%) in the coflow. In a practical system such as that of a jet-in-hot-coflow combustion system, the coflow generates a boundary layer over the outer wall of the jet pipe and this may have a significant effect on the evolution of the flow field in the NIF, having an impact on the mixing and other reacting phenomenon. The flow field of a turbulent jet in turbulent coflow was measured by 2D2C PIV in the region $0 \leq x/D \leq 40$ for coflow ratios of 0, 0.09, 0.16, and 0.33. The first point of interest is to see whether a jet-in-coflow may be represented as an effectively slow-moving free jet by applying the appropriate scaling. An overview of the flowfield is presented in terms of the mean axial velocity and turbulence intensity distribution, along with centerline profiles for mean velocity, jet half-width, and jet momentum. The centerline profiles of the scaled jet-in-coflow cases differ from those of a free jet. Increasing the coflow ratio leads to a lower centerline mean velocity decay rate, reduced jet spreading, and a virtual origin shift upstream toward the nozzle compared to a free jet. Further, the turbulent coflow contributes an addition of axial momentum to the turbulent jet along the axis.

To investigate the cause for these deviations, radial profiles of one-point velocity statistics are plotted at x/D=5, 10, 22, and 30. For cases of higher coflow ratio, there is a clear axial velocity deficit in the interface region. The mean profiles of turbulence intensity and RSS show a higher peak near one halfwidth distance from the jet center. The velocity deficit is attributed to the coflow initial conditions where a boundary layer is formed on the external wall of the pipe producing the jet. To get a better understanding of the interaction between the jet and the turbulent coflow at the interface, conditional statistics are assembled with respect to the instantaneous interface detected in the PIV image frames. The velocity deficit at the interface for the jet-in-coflow is also seen in the conditional axial velocity profiles. This is postulated to originate from the boundary layer generated over the outer wall of the jet pipe. The turbulence of the coflow has little effect on the structure of the interface as is seen from the enstrophy diffusion peak profile, which has a similar structure for the various jet-in-coflow cases and the free jet case. On the other hand, the enstrophy dissipation has a lower magnitude for the jet-in-coflow cases, correlating well with the higher peak levels of RSS and enstrophy on the jet side of the interface, compared to the free jet case. Thus, the higher peaks of turbulence, also seen in the mean radial profiles, is attributed to reduced dissipation in the jet-in-coflow due to the "shielding effect" of the wake of the boundary layer initially formed around the jet pipe. Further, the tortuosity of the interface is found to be lower for the jet-in-coflow compared to the free jet, which shows that the low turbulence intensity of the coflow cannot contort the interface, and the "shielding effect" dampens the contortion that may arise.

This work was motivated by the need to understand the turbulent flow fields in MILD/Flameless combustion systems, but since this was done in a isothermal flow field, it is recommended to verify the applicability of these results under conditions with heat release.

Acknowledgements RS would like to thank Simon Vermeijlen for their help during the experiment campaign.

Data Availability The measured data will be made available on the 4TU.ResearchData repository.

References

Antonia, R.A., Bilger, R.W.: An experimental investigation of an axisymmetric jet in a co-flowing air stream. J. Fluid Mech. **61**(4), 805–822 (1973). https://doi.org/10.1017/S0022112073000959

Balamurugan, G., Rodda, A., Philip, J., et al.: Characteristics of the turbulent non-turbulent interface in a spatially evolving turbulent mixinga layer. J. Fluid Mech. (2020). https://doi.org/10.1017/jfm.2020.241

Ball, C.G., Fellouah, H., Pollard, A.: The flow field in turbulent round free jets. Prog. Aerosp. Sci. **50**, 1–26 (2012). https://doi.org/10.1016/j.paerosci.2011.10.002

Bisset, D.K., Hunt, J.C., Rogers, M.M.: The turbulent/non-turbulent interface bounding a far wake. J. Fluid Mech. **451**, 383–410 (2002). https://doi.org/10.1017/s0022112001006759

Bradski, G.: The OpenCV Library. Dr Dobb's Journal of Software Tools (2000)

Cabra, R., Chen, J.Y., Dibble, R.W., et al.: Lifted methane-air jet flames in a vitiated coflow. Combust. Flame **143**(4), 491–506 (2005). https://doi.org/10.1016/j.combustflame.2005.08.019

Chauhan, K., Philip, J., De Silva, C.M., et al.: The turbulent/non-turbulent interface and entrainment in a boundary layer. J. Fluid Mech. **742**, 119–151 (2014). https://doi.org/10.1017/jfm.2013.641

Chen, J., Buxton, O.R.: Spatial evolution of the turbulent/turbulent interface geometry in a cylinder wake. Journal of Fluid Mechanics **969**, 1–23 (2023) https://doi.org/10.1017/jfm.2023.547, arXiv:2301.04959

Chu, P., Lee, J.H., Chu, V.H.: Three-Dimensional Salinity Simulations of. J. Hydraul. Eng. **125**, 193–204 (1999). https://doi.org/10.1061/(ASCE)0733-9429(1999)125

Corrsin, S., Kistler, A.L.: Free-Stream Boundaries of Turbulent Flows. Tech. rep (1955)

Da Silva, C.B., Dos Reis, R.J.: The role of coherent vortices near the turbulent / non-turbulent interface. Philos. Trans. the Royal Soc. London Series A: Phys. Eng. Sci. **368**, 738–753 (2011). https://doi.org/10.1098/rsta.2010.0300

Da Silva, C.B., Taveira, R.R.: The thickness of the turbulent/nonturbulent interface is equal to the radius of the large vorticity structures near the edge of the shear layer. Phys. Fluids **10**(1063/1), 3527548 (2010)

Da Silva, C.B., Hunt, J.C., Eames, I., et al.: Interfacial layers between regions of different turbulence intensity. Annu. Rev. Fluid Mech. **46**, 567–590 (2014). https://doi.org/10.1146/annurev-fluid-010313-141357

Dahm, W., Dibble, R.: Combustion stability limits of coflowing turbulent jet diffusion flames. In: 26th Aerospace Sciences Meeting. American Institute of Aeronautics and Astronautics, Reston, Virigina, https://doi.org/10.2514/6.1988-538 (1988)

Dimotakis, P.E.: The mixing transition in turbulent flows. J. Fluid Mech. **409**, 69–98 (2000). https://doi.org/10.1017/S0022112099007946

Elsinga, G.E., Adrian, R.J., Van Oudheusden, B.W., et al.: Three-dimensional vortex organization in a high-Reynolds-number supersonic turbulent boundary layer. J. Fluid Mech. **644**, 35–60 (2010). https://doi.org/10.1017/S0022112009992047

Ganapathisubramani, B., Lakshminarasimhan, K., Clemens, N.T.: Determination of complete velocity gradient tensor by using cinematographic stereoscopic PIV in a turbulent jet. Exp. Fluids **42**(6), 923–939 (2007). https://doi.org/10.1007/s00348-007-0303-5

Gaskin, S., Wood, I.: The axisymmetric and the plane jet in a coflow. J. Hydraul. Res. **39**(5), 451–458 (2001). https://doi.org/10.1080/00221686.2001.9628270

Gaskin, S.J., McKernan, M., Xue, F.: The effect of background turbulence on jet entrainment: an experimental study of a plane jet in a shallow coflow. J. Hydraul. Res. **42**(5), 533–542 (2004). https://doi.org/10.1080/00221686.2004.9641222

Hussein, H.J., Capp, S.P., George, W.K.: Velocity measurements in a high-Reynolds-number, momentum-conserving, axisymmetric, turbulent jet. J. Fluid Mech. **258**, 31–75 (1994)

Kankanwadi, K.S., Buxton, O.R.: Turbulent entrainment into a cylinder wake from a turbulent background. J. Fluid Mech. (2020). https://doi.org/10.1017/jfm.2020.755

Kankanwadi, K.S., Buxton, O.R.: On the physical nature of the turbulent/turbulent interface. J. Fluid Mech. **942**, 1–14 (2022). https://doi.org/10.1017/jfm.2022.388

Khashehchi, M., Ooi, A., Soria, J., et al.: Evolution of the turbulent/non-turbulent interface of an axisymmetric turbulent jet. Exp. Fluids **54**(1), 1449 (2013). https://doi.org/10.1007/s00348-012-1449-3

Khorsandi, B., Gaskin, S., Mydlarski, L.: Effect of background turbulence on an axisymmetric turbulent jet. J. Fluid Mech. **736**, 250–286 (2013). https://doi.org/10.1017/jfm.2013.465

Kohan, K.F., Gaskin, S.J.: On the scalar turbulent/turbulent interface of axisymmetric jets. J. Fluid Mech. **950**, 1–17 (2022). https://doi.org/10.1017/jfm.2022.825

Kurian, T., Fransson, J.H.: Grid-generated turbulence revisited. Fluid Dyn. Res. (2009). https://doi.org/10.1088/0169-5983/41/2/021403

Mistry, D., Philip, J., Dawson, J.R., et al.: Entrainment at multi-scales across the turbulent/non-turbulent interface in an axisymmetric jet. J. Fluid Mech. **802**, 690–725 (2016). https://doi.org/10.1017/jfm.2016.474

Moeini, M., Khorsandi, B., Mydlarski, L.: Effect of Coflow turbulence on the dynamics and mixing of a nonbuoyant turbulent jet. J. Hydraul. Eng. **147**(1), 1–13 (2021). https://doi.org/10.1061/(asce)hy.1943-7900.0001830

Morton, B.R., Geoffrey, T., Turner, J.S.: Turbulent Gravitational Convection from Maintained and Instantaneous Sources. In: Proceedings of the Royal Society of London. Series A, Mathematical and Physical, pp 1–23 (1956)

Nickels, T.B., Perry, A.E.: An experimental and theoretical study of the turbulent coflowing jet. J. Fluid Mech. **309**, 157–182 (1996). https://doi.org/10.1017/S0022112096001590

Oldenhof, E., Tummers, M.J., van Veen, E.H., et al.: Role of entrainment in the stabilisation of jet-in-hot-coflow flames. Combust. Flame **158**(8), 1553–1563 (2011). https://doi.org/10.1016/j.combustflame.2010.12.018

Or, C., Lam, K., Liu, P.: Potential core lengths of round jets in stagnant and moving environments. J. Hydro-Environ. Res. **5**(2), 81–91 (2011). https://doi.org/10.1016/j.jher.2011.01.002

Panchapakesan, N.R., Lumley, J.L.: Turbulence measurements in axisymmetric jets of air and helium. Part 2. helium jet. J. Fluid Mech. **246**, 225–247 (1993). https://doi.org/10.1017/S0022112093000102

Prasad, R.R., Sreenivasan, K.R.: Scalar interfaces in digital images of turbulent flows. Exp. Fluids **7**(2–3), 259–264 (1989). https://doi.org/10.1007/s00348-007-0370-7

Roshko, A.: On the development of turbulent wakes from vortex streets. Tech. rep., NACA, https://ntrs.nasa.gov/citations/19930092207 (1954)

Sahebjam, R., Kohan, K.F., Gaskin, S.: The dynamics of an axisymmetric turbulent jet in ambient turbulence interpreted from the passive scalar field statistics. Phys. Fluids **10**(1063/5), 0071023 (2022)

Schubert, E., Sander, J., Ester, M., et al.: DBSCAN revisited, revisited: why and how you should (still) use DBSCAN. ACM Trans. Database Syst. (2017). https://doi.org/10.1145/3068335

da Silva, C.B., Pereira, J.C.: Invariants of the velocity-gradient, rate-of-strain, and rate-of-rotation tensors across the turbulent/nonturbulent interface in jets. Phys. Fluids **10**(1063/1), 2912513 (2008)

Taveira, R.R., da Silva, C.B.: Kinetic energy budgets near the turbulent/nonturbulent interface in jets. Phys. Fluids **10**(1063/1), 4776780 (2013)

Taveira, R.R., da Silva, C.B.: Characteristics of the viscous superlayer in shear free turbulence and in planar turbulent jets. Phys. Fluids **10**(1063/1), 4866456 (2014)

Uddin, M., Pollard, A.: Self-similarity of coflowing jets: the virtual origin. Phys. Fluids **19**(6), 068103 (2007). https://doi.org/10.1063/1.2740709

Vita, G., Hemida, H., Andrianne, T., et al.: Generating atmospheric turbulence using passive grids in an expansion test section of a wind tunnel. J. Wind Eng. Ind. Aerodyn. **178**(February), 91–104 (2018). https://doi.org/10.1016/j.jweia.2018.02.007

Watanabe, T., Sakai, Y., Nagata, K., et al.: Turbulent mixing of passive scalar near turbulent and non-turbulent interface in mixing layers. Phys. Fluids **10**(1063/1), 4928199 (2015)

Watanabe, T., Zhang, X., Nagata, K.: Turbulent/non-turbulent interfaces detected in DNS of incompressible turbulent boundary layers. Physics of Fluids 30 (3) (2018)https://doi.org/10.1063/1.5022423

Westerweel, J., Fukushima, C., Pedersen, J.M., et al.: Momentum and scalar transport at the turbulent/non-turbulent interface of a jet. J. Fluid Mech. **631**, 199–230 (2009). https://doi.org/10.1017/S0022112009006600

Wygnanski, I., Fiedler, H.: Some measurements in the self-preserving jet. J. Fluid Mech. **38**, 577–612 (1969)

Xu, G., Antonia, R.A.: Effect of different initial conditions on a turbulent round free jet. Exp. Fluids **33**(5), 677–683 (2002). https://doi.org/10.1007/s00348-002-0523-7

Zhang, X., Chin, R.C.: A numerical study of the effects of the velocity ratio on Coflow jet characteristics. J. Fluids Eng, Trans. ASME **142**(8), 1–13 (2020). https://doi.org/10.1115/1.4046769